TRANSMISSION WELDING OF GLASSES BY FEMTOSECOND LASER: STRUCTURAL AND MECHANICAL PROPERTIES

Paper M1002

Panjawat Kongsuwan, Y. Lawrence Yao

Columbia University, New York, NY, 10027, USA

Abstract

Femtosecond laser pulses were focused on the interface of two glass specimens. Proper use of optical and laser processing parameters enables transmission welding. The morphology of the weld cross section was studied using differential interference contrast optical microscopy. The changes in mechanical properties of the weld seams were studied through spatially resolved nanoindentation, and indentation fracture analysis was used to investigate the strength of the weld seams. In addition, a numerical model was developed to predict the absorption volumes of femtosecond laser pulses inside a transparent material. The model takes into account the temporal and spatial characteristics and propagation properties of the laser beam, and the transmission welding widths were subsequently compared with the absorption widths predicted by the model.

Introduction

Glasses are widely used in various flat panel displays and biomedical applications. Joining techniques of glasses are usually based on adhesive agent or interlayer. Laser beam welding is considered to be one of highly flexible techniques for joining glass. The main advantages of laser welding are that the energy is supplied contactless and can be directly coupled in the joining zone. However, due to high transmission of light through these transparent materials, glass-glass joining by conventional laser requires interlayer or opaque material between the top and bottom pieces to absorb laser energy. However, due to non-linear absorption characteristic of femtosecond laser, transmission welding of both transparent materials is possible when the laser beam is tightly focused on the interface between two glass plates.

Two different regimes of transmission welding by ultrashort pulse laser have been identified. The low repetition rate regime (1-200 kHz) and high repetition rate regime (>200 kHz) depending on whether the time interval between successive pulses is longer or shorter than the characteristic time that heat diffuses outside the focal volume [1]. Tamaki et al. [2] first demonstrated the welding between two silica glass plates without a light-absorbent intermediate layer using low repetition rate femtosecond laser. Watanabe et al. [3] then reported on the welding of dissimilar transparent materials using the same laser, and also investigated the parameters that resulted in joining by varying the laser pulse energy and the translation velocity. However, there has been no morphology study of the weld seam and no clear welding cross section figure in this low repetition rate regime. Tamaki et al. [4] also reported on laser micro-welding of transparent materials based on a localized heat accumulation effect using high repetition rate femtosecond laser, and performed a simple tensile test after welding to estimate the joint strength. However, the testing procedure was not precise due to inability to continuously increase the applied load. Later on, there are more reports [5-7] on the possibility of ultrashort pulse laser welding of borosilicate glass substrates in the high repetition rate regime. However, there has been no quantitative evaluation of joint strength and no mechanical property study of the weld seam.

There are many attempts to simplify the problem by characterizing mechanical properties of the molten region irradiated by ultrashort pulse laser inside a single piece of transparent materials. Miyamoto et al. [8] evaluated the mechanical strength of laser-melt zone using a three-point bending test, and showed that the strength in that zone was as high as un-irradiated base material; however, the sample had to be polished to unveil the laser induced feature at the bottom surface in order to experience the maximum tensile stress. Borrelli et al. [9] performed a double torsion test to measure fracture toughness, and revealed that the apparent fracture toughness is increased within the laser-treated area due to strengthening effect. Bellouard et al. [10] used nanoindentation tests to show an increase in Young's modulus within the laser treated zones of fused silica irradiated by femtosecond pulses with high repetition rate; however, these measurements were not constrained to within the treated regions. Kongsuwan et al. [11] performed spatially resolved nanoindentation test and revealed a

decrease in Young's Modulus and hardness, and an increase in ductility in treated regions of fused silica irradiated by femtosecond laser pulses with low repetition rate; however, the mechanical properties and strength of real weld seams instead of features inside single-piece specimens are still required further investigation.

In this paper, transmission welding using femtosecond laser with low repetition rate has been performed to study the morphology and mechanical properties in the welding zone. A role and effect of the gap at the interface between two transparent material plates on the welding and a joining mechanism of low repetition rate femtosecond laser have also been investigated. Differential interference contrast optical microscopy is employed to study the morphology of the weld cross section, and it will also be compared with the results from a developed numerical model. Spatially resolved nanoindentation will be used to study the mechanical properties and the strength of the weld seams.

Background

Femtosecond Laser Interaction with Transparent Materials

For transmission welding, due to Gaussian temporal profile of a femtosecond laser pulse, when a laser beam is tightly focused by objective lens below and close to the interface of two glass plates the leading edge of the converging laser pulse starts breakdown the material at or above the focal plane when the intensity reaches the material breakdown threshold, and the subsequent temporal slices of the laser pulse with higher intensity then produce breakdown upward where the beam diameter is larger [12-13] leading to the teardrop-shaped absorption volume. Since breakdown threshold of air is less than that of glasses, both glasses and air are ionized inside the absorption volume. The shape of this volume is assumed top-half ellipsoid and bottom-half conical frustum, and its volume, V_{abs}, surface area, S_{abs}, and lateral (w_{xy}) and axial (w_z) $1/e^2$ radii are approximately equal to:

$$V_{abs} = \frac{1}{2}\times\frac{4}{3}w_{xy}^2 w_z + \frac{\pi w_z}{3}(w_{xy}^2 + w_{xy}w_0 + w_0^2) \quad (1)$$

$$S_{abs} \approx 4\pi(w_{xy}^{2p} + 2w_{xy}^p w_z^p)^{1/p} + \pi(w_{xy}+w_0)\sqrt{(w_{xy}-w_0)^2 + w_z^2} \quad (2)$$

$$w_{xy} = \sqrt{\frac{2P_0 e^{-2}}{\pi I_{th}}}; \qquad w_z = \frac{\pi w_0^2}{2M^2\lambda}\sqrt{\frac{2P_0}{I_{th}\pi w_0^2} - 1} \quad (3)$$

where w_0 is diffraction-limited lateral radius, p is the constant ($\approx$ 1.6075), P_0 is the peak power, I_{th} is the intensity threshold of materials, M^2 is the laser quality factor, and λ is the laser wavelength.

At the end of femtosecond laser pulse duration, the laser energy absorption process is completed, and hot electron plasma will be semi-confined within the absorption volume of which the surface area is partially exposed to the air gap between the two plates. When the electrons have transferred their energy to ions, the hydrodynamic motion starts, and the shock wave emerges from the energy deposition zone [14]. The total deposited energy density, Q_{dep}, build up the pressure gradient in the absorption volume that drives the shock wave, the average pressure, P_{avg}, in this volume can be calculated as [15].

$$P_{avg} \approx Q_{dep} = \frac{AE_p}{V_{abs}} \quad (4)$$

where A is the absorption coefficient, E_p is the laser pulse energy. This pressure are considerably higher than the van der Waals force between two parallel transparent material plates pressed together to have a very small gap (1-2 μm). The van der Waals force per unit area, F_{vdw}, is given by Eq.(6) [16]. Although the plates are clamped on both sides, due to these shock pressures, the gap at the interface is open wider equal to the deflection, δ, in Eq.(7) considering model of beam simply supported at both ends and subjected to a concentrated load at any point [17].

$$F_{vdw} = \frac{0.162hc}{d^4\pi^3}\left(\frac{n_\infty^2 - 1}{n_\infty^2 + 2}\right)^2 \quad (5)$$

$$\delta = \frac{2[(P_{avg} - F_{vdw})\pi w_{xy}^2]ba(l^2 - a^2 - b^2)}{6lEI} \quad (6)$$

where d is the distance between plates, h is the Planck's constant, c is the speed of light, n_∞ is the refractive index of the plates at infinite wavelength, l is the distance between both supported ends, a and b are the distance from the load point to each supported end, E is the Young's modulus of materials, I is the area moment of inertia.

The shock wave generating inside the absorption volume will propagate to all directions. Most of the shock wave propagating directions is confined within a cold material; therefore, most of the material inside the absorption volume is compressed and transformed into a post-shock state. However, some shock wave propagating directions are toward the open space of air gap at the interface between two plates. Thus, there is small fraction of mass transporting from the absorption volume to the air gap in its surrounding region.

Mechanical Properties and Strength of the Weld Seam

Obviously, the material in transmission welding region possesses properties different from that in the initial state. Depend on applications, the weld seams may subject to different types of loading such as tension, shear, and etc. For ductile materials, weld strength is typically determined using tensile tests, shear tests, torque tests, and etc. However, for brittle materials such as glasses, they deform elastically up to failure without permanent deformation under the action of tensile stress, and the fracture begins in a direction approximately perpendicular to the maximum tensile stress. Therefore, fracture mechanic analysis may be used as a tool to identify the weld strength as well. Mode I (opening mode) of fracture, which is a failure due to tensile stress, is the most applicable to glasses since they generally fail in tension, which is more likely the loading type in flat panel display application. From Griffith's analysis under tensile stress, the strength of a flawed brittle solid, σ_f, is given by [18]:

$$\sigma_f = \sqrt{2E\gamma/\pi c} \tag{7}$$

where E is the modulus of elasticity, γ is the free surface energy, and c is the crack length.

It may realized from Eq.(7) that $\sigma_f\sqrt{\pi c} = \sqrt{2E\gamma}$ = constant, depending upon the material and its environment [19]. In mode I under applied stress, σ_a, the stress intensity factor, $K_I = \sigma_a\sqrt{\pi c}$, is defined, and the fracture toughness or the critical stress intensity factor, $K_{IC} = \sigma_f\sqrt{\pi c}$, is thus a physical characteristic of the material. The fracture would occur when $K_I \to K_{IC}$. It is widely accepted that K_{IC} can be obtained by measuring the post-indentation radial crack size emanating from the indent as a function of load as given in Eq. (8) [20]

$$K_{IC} = \xi_0(\cot\Phi)^{2/3}(\frac{E}{H})^{1/2}\frac{P}{c^{3/2}} \tag{8}$$

where ξ_0 is the dimensionless constant, Φ is the indenter half-angle, E and H are the indentation Young's modulus and hardness of the material, P is the peak indentation load, and c is the crack length. Lower E/H corresponds to lower hoop-tensile residual field intensity, implying a stronger elastic recovery and thus more pronounced radial extension during the unloading half-cycle [20].

Hardness of a glass can influence the practical strength through its influence on the resistance to flaw formation [21]. Therefore, the hardness profile of a weld is often shown as an estimate of tensile strength [22]. The elastic modulus of glasses is related to bond strength, and it is higher for glass with a more rigid structure. Although further investigation is needed, it is interesting that the hardness (H), the modulus (E), and the elastic-plastic ratio (E/H) at the weld region may reflect transmission welding strength of transparent materials.

Numerical Analysis of Absorption Volume

Based on fundamental of laser beams and optics, in order to accurately capture absorption volume shape, the numerical model should be constructed by considering the Gaussian temporal distribution of laser power, $P(t)$, in laser pulse duration as given in Eq. (9) and considering the Gaussian spatial distribution of laser intensity, $I(x,y,t)$, with $1/e^2$ radius of unfocused beam, R_0, as given in Eq. (10).

$$P(t) = \frac{E_p\sqrt{4\ln 2}}{\sqrt{\pi}t_p}\exp[-4\ln 2(\frac{t-t_p}{t_p})^2] \tag{9}$$

$$I(x,y,t) = \frac{2P(t)}{\pi R_0^{\,2}}\exp[\frac{-2r^2}{R_0^{\,2}}] \tag{10}$$

where E_p is the laser pulse energy, t_p is FWHM pulse duration, $r = \sqrt{x^2+y^2}$ is the distance from the center of laser beam, and t is time. The laser beam with intensity corresponding to Eq. (10) focused by an objective lens will be converged to a diffraction-limited spot size, and the variation in size of converging laser beam can be calculated by Eq. (11).

$$w(z) = w_0[1+(\frac{M^2\lambda z}{\pi w_0^{\,2}})^2]^{1/2}; \qquad w_0 = \frac{0.32\lambda}{NA} \tag{11}$$

where w_0 is diffraction-limited radius, λ is the laser wavelength, NA is the numerical aperture of an objective lens, M^2 is the laser quality factor, z is the distance from laser focal plane.

Once the laser intensity at each time slice in Eq. (9) is focused into the material to the positions that their absorbed intensities are condensed enough comparable to the intensity threshold, I_{th}, of the material given by Eq. (12) [23], there are breakdown, and plasma is assumed to be formed at those positions. The breakdown will be generated upward during the first half of pulse duration to form the absorption volume, and the energy in the second half of pulse duration will be absorbed in this absorption volume to generate higher-density plasma in the absorption volume.

$$I_{th} = \left(\frac{n_c}{n_a \tau_{rec} \beta_{mpi}}\right)^{1/n_{ph}} \quad (12)$$

where n_c is the electron critical density, n_a is the density of neutral atoms, β_{mpi} is the field ionization coefficient, and n_{ph} is the number of absorbed photons.

Experimental Setup and Characterization

Transmission welding is achieved by using a chirped amplified Ti:Sapphire laser system which outputs high energy ultrashort pulses with 800 nm wavelength and 130 fs pulse duration at a 1 kHz repetition rate. The commercial grade borosilicate glass (BK7) of 1.0 mm thick was cut to approximately 6 mm x 12 mm size and then cleaned by RCA-cleaning [24], subsequently pressed together at around 2 MPa for 10 min, and clamped on the both ends before fixing on a motorized linear stage and processing by femtosecond laser pulses. The laser beam was focused by 40x objective lens with *NA* 0.60 onto the interface between the plates. A schematic diagram of the experimental setup is illustrated in Fig. 1. Different conditions of laser processing parameters were applied by varying the feed rate of the stage and the energy of the laser pulses.

After the femtosecond laser treatment, the samples were then ground with carbide papers and polished with cerium-oxide and a leather polishing pad to have smooth surface. Reflective light differential interference contrast (DIC) optical microscopy, which can reveal more contrast and details in the feature morphology was used to obtain the cross section view of the weld seams. The welding zone was examined via nanoindentation using a three-sided Berkovich indenter tip to characterize the mechanical properties.

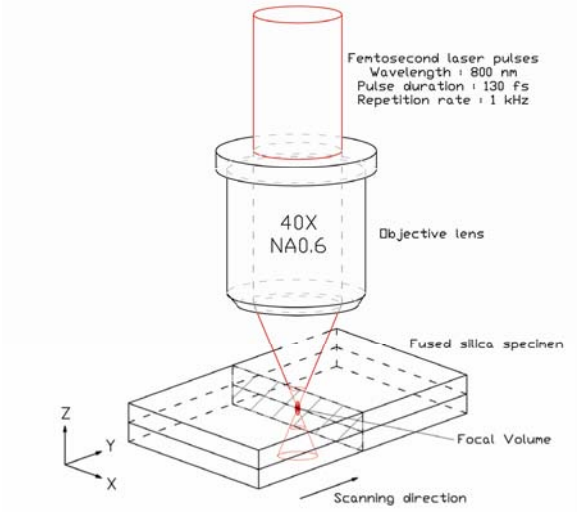

Figure 1: Schematic illustration of experimental setup. The laser beam is focused onto the interface of two borosilicate glass plates, and the scanning direction is along the y-axis.

100 nm depth spatially resolved nanoindents with 3 μm spacing in the x and z directions were conducted to cover the cross section of both the welding zone and a nearby unaffected region. 150gf load nanoindents were also performed on the features to induce cracks in order to investigate the change in fracture toughness of the welding zones. Different laser pulse energy conditions were used to investigate the effects of laser pulse energy on morphology and mechanical properties of the weld seams.

Results and Discussion

Welding Morphology

Other studies [6-8] used the high precision flatness of glass plates and mentioned the gap need to be less than λ/4 in order that the welding to be succeeded. However, BK7 glass plates with standard flatness of 3-5 waves/inch was used in this study. The welding is successfully performed, and Fig. 2 shows transmission welding cross section of two BK7 glass plates from reflective DIC optical microscopy. There is continuity of the material from the top piece to the bottom piece in welding region. From this figure, it can also be observed that the shape of an affected region is a teardrop shape and it looks similar to the morphology of femtosecond laser modification inside single piece of a material [11]. AFM topography was also carried out to image cross section profiles across both welding and reference regions as shown in Fig. 3. It is very clear that the two borosilicate glass plates were joined together although the gap between the plates is not as low as λ/4.

For a mechanism of transmission welding seam formation in case of using low repetition rate regime of femtosecond laser pulse, due to its low repetition rate and the presence of the air gap at the interface, the pressure evolution inside the absorption volume will play an important role in welding seam formation.

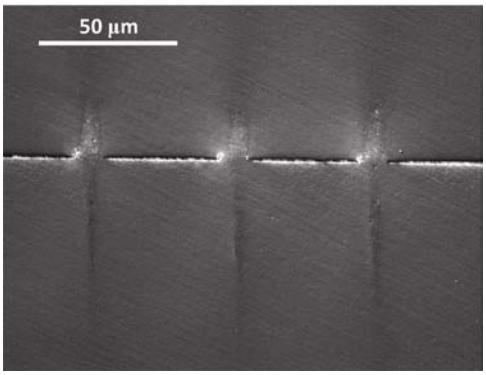

Figure 2: Reflective DIC optical microscopy of cross section view (x-z plane) of a welding seam (laser pulse energy of 10 μJ, scanning speed of 0.02 mm/s, and rep rate of 1 kHz.)

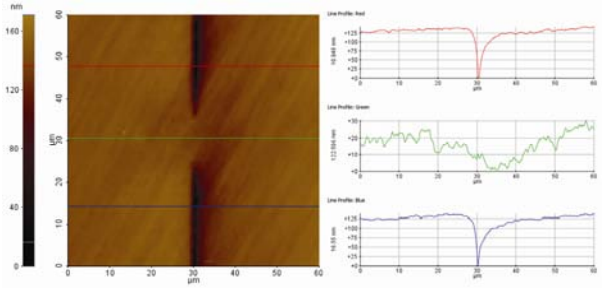

Figure 3: AFM topography of a welding seam in Fig. 2.

The material and air inside the absorption volume that were ionized to experience high temperature and high pressure will be eventually compressed and transformed into the welding and affected regions. According to Eq. (1) and (2), in case of 10 μJ pulse energy, the absorption volume is approximated 6.84 x 10^{-16} m^3, and the surface area of this absorption volume is approximated 4.18 x 10^{-10} m^2. The average pressure of 14.6 GPa, which calculated from Eq. (3), is assumed to be generated inside the absorption volume. From Eq. (5), this pressure causes the deflection of the plates around 43.5 nm if the welding line distance 1 mm from a supported end or 466 nm if the welding line locates at the center between the supported ends. Assuming the initial gap is equal to 1.5 μm, the gap will be opened wider, and the surface area of the absorption volume is semi-confined with approximately 10% of the area exposed to the open space. Therefore, it depends on the average pressure, the pressure gradient, and the open-space area, some small fraction of post-shock state material would possibly be driven out of the absorption volume to the surrounding area at the interface between the plates as debris.

To verify this mechanism, the top view of welding lines with different pulse energies shown in Fig.4, was analysed. There are four distinctive lines in this figure with the processing conditions of increasing laser pulse energy from the leftmost to the rightmost line. For the first welding line on the left, since the top portion of absorption volume lies on the interface, the pressure gradient in directions that confined within the material was stronger than in the directions that open to space, and the debris was left close to the welding line. On the other hand, for the second welding line, due to high enough average pressure and strong pressure gradient in the directions open to space, the debris was driven farther and scattering debris was found quite far away from the second welding line. When the laser pulse energy is further increased as the condition of the third welding line from the left, the average pressure, the pressure gradient, and the unconfined area are all decreased such that surrounding the welding line, the debris was rarely seen. For the last welding line on the right, although the laser pulse energy is the highest of

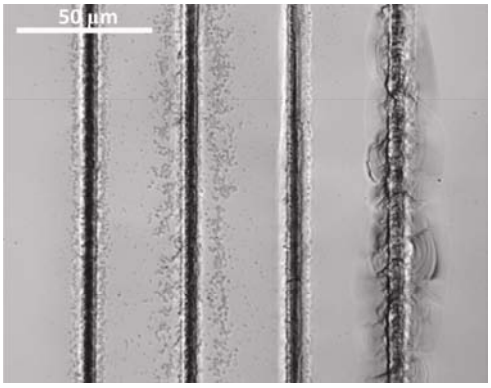

Figure 4: Transmission DIC optical microscopy of top view of different-condition welding lines (laser pulse energy of 10 μJ, 20 μJ, 30 μJ, and 50 μJ respectively from the left, scanning speed of 0.02 mm/s, and repetition rate of 1 kHz.)

the four conditions, the average pressure is the lowest, and the pressure gradient is too low to drive the debris out from the absorption volume. However, the local pressure in this condition is higher than that in the other conditions such that many cracks were induced near the welding line as shown in Fig. 4.

The effect of laser pulse energy on the welding width is shown in Fig. 5. From the experimental result at different pulse energy, the width of welding lines was increased when increasing laser pulse energy. From Eq. (3), the width of absorption volume depends on peak power or laser pulse energy; therefore, for higher pulse energy, the materials inside the larger absorption volume will be transformed into the bigger welding and affected regions. The welding width may be larger than the width of absorption volume due to multiple pulse effect, but it should have the same order of magnitude in size with the width of absorption volume, and it should increase in size when the laser pulse energy was increased as clearly seen in Fig. 5.

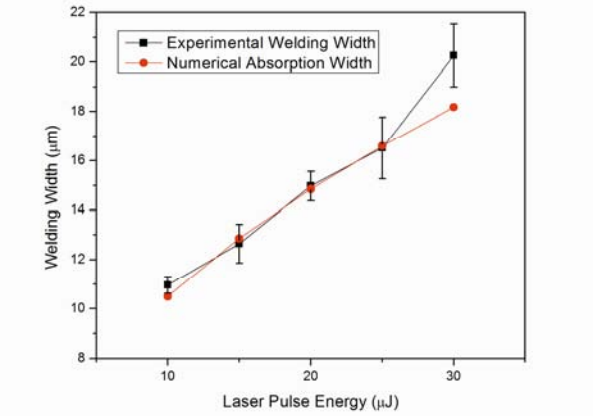

Figure 5: Comparison of experimental welding width and numerical absorption width in transmission welding of borosilicate glass plates at different laser pulse energies. Error bars denote standard deviation.

Absorption Volume Modeling

To model the absorption volume shape, one should consider both temporal and spatial distribution characteristics of femtosecond laser pulses, and also account for the focusing characteristics of collimated laser beam through transparent materials. Fig.6 illustrates the schematic flow diagram of the absorption volume modeling. From an known amount of laser pulse energy, a full-width-at-half-maximum (FWHM) pulse width, and the assumption of Gaussian temporal profile of femtosecond laser pulse, the distribution of power in laser pulse duration can be determined by Eq. (9). Subsequently, using Eq. (10), the distribution of intensity in unfocused laser spot can be calculated from each temporal slide of power, $1/e^2$ radius of unfocused beam, and the assumption of Gaussian spatial profile of femtosecond laser pulse. From the laser intensity at any locations within the unfocused laser beam and the intensity threshold of transparent material, the breakdown points in lateral direction of converging laser beam could be derived by considering how intense the area should be in order that the intensity at those locations will reach the material intensity threshold. Consequently, the breakdown points in optical axis can be determined from each breakdown points in radial axis, the diffraction-limited spot size and the variation in size of converging laser beam by an objective lens using Eq. (11). The breakdown points in each temporal slice form the concave-down parabolic line, and breakdown lines in full temporal profile eventually form the absorption volume as shown in Fig. 7(a) and Fig. 8(a). Assuming the small air gap between the interface, and ignoring the reflection at the interface, this model is applicable for transmission welding as well as inside single piece.

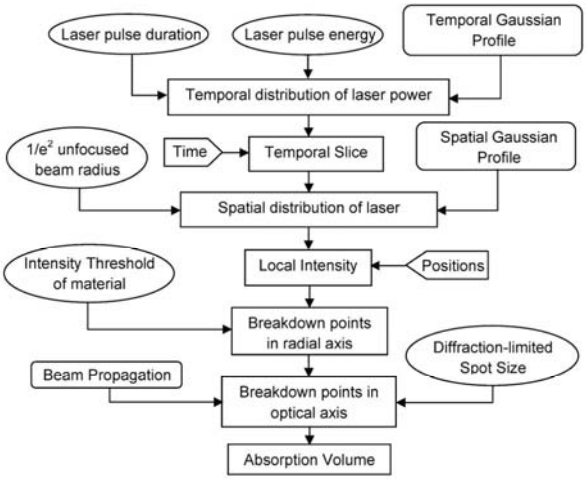

Figure 6: Schematic diagram of absorption volume modeling.

Fig. 7(a) shows cross section of the absorption volume at different laser pulse energies. The cross section shape of the absorption volume indeed looks like the teardrop shape. The width and height of cross section are greater with increasing laser pulse energy corresponding to the experimental results in other studies [11-13]. Higher laser pulse energy leads to higher peak power, which generates higher local intensity. Consequently, the breakdown points of the material will be farther from the center in the radial axis, and will also be farther from the focal plane in the optical axis. Therefore, the height and width of the absorption volume in high laser pulse energy are greater than low laser pulse energy as shown in Fig. 7(b). The widths of absorption volume at different laser pulse energies were also compared to the experimental welding widths in Fig. 5. The numerical widths had the same order of magnitude with the experimental ones, and they followed the same trend of increasing width for higher laser pulse energy. Therefore, the absorption volume model could give the user an idea how big the welding width he will get by using designed pulse energy. For the aspect ratio of the absorption volume, it is more-or-less constant corresponding to the aspect ratio of the experimental features in previous study [11], and also corresponding to the aspect ratio of focal volume using the illumination point spread function, of which the ratio is constant and independent of laser pulse energy [25].

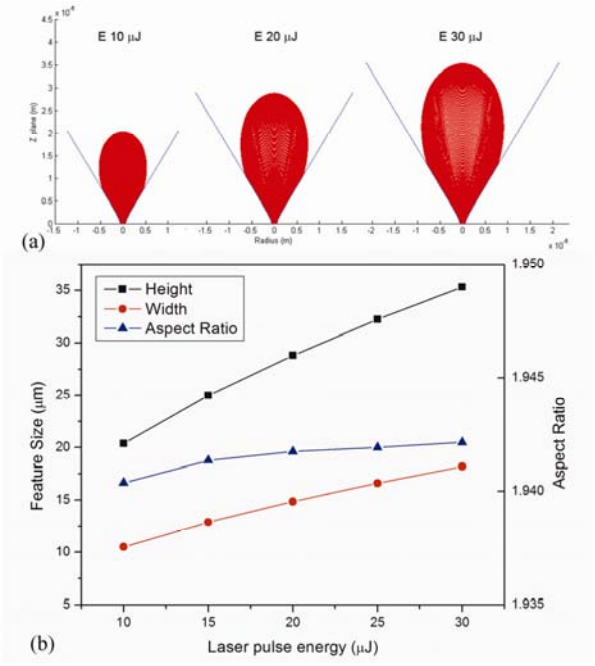

Figure 7: (a) Cross section view (b) height, width, and height/width ratio of absorption volume at different laser pulse energies (NA 0.6)

Fig. 8(a) shows the cross section of the absorption volume using different numerical apertures (NAs) of objective lens. For high NA, the teardrop shape of the absorption volume tends to have more-or-less equivalent size in height and width corresponding to the experimental results of Schaffer et al. [12]. Using high NA, laser beam is more tightly focused to a smaller diffraction-limited spot size as given in Eq. (11). For each temporal slice of fixed laser pulse energy, the intensity of any points within the unfocused beam will reach the material intensity threshold when the laser beam is focused down to a smaller spot, and their breakdown locations in the radial axis are not changed. Therefore, the widths of absorption volumes are constant and independent of NAs as shown in Fig. 8(b). However, their corresponding breakdown points of material in the optical axis depend on the diffraction-limited spot size and the converging angle of focused laser beam. For higher NAs, the unfocused laser beam is converged faster to the diffraction-limited spot size at the focusing plane; therefore, at same breakdown points in the radial axis, their corresponding breakdown points in the optical axis are closer to the focusing plane. The heights of absorption volumes are thus decreased with higher NAs as shown in Fig. 8(b). For the aspect ratio of the absorption volume, it is decreased with higher NAs corresponding well with the aspect ratio of the experimental features studied by Schaffer et al. [12]. The shape, size and aspect ratio from this absorption volume model thus better reflect the experimental results than using the focal volume of illumination point spread function.

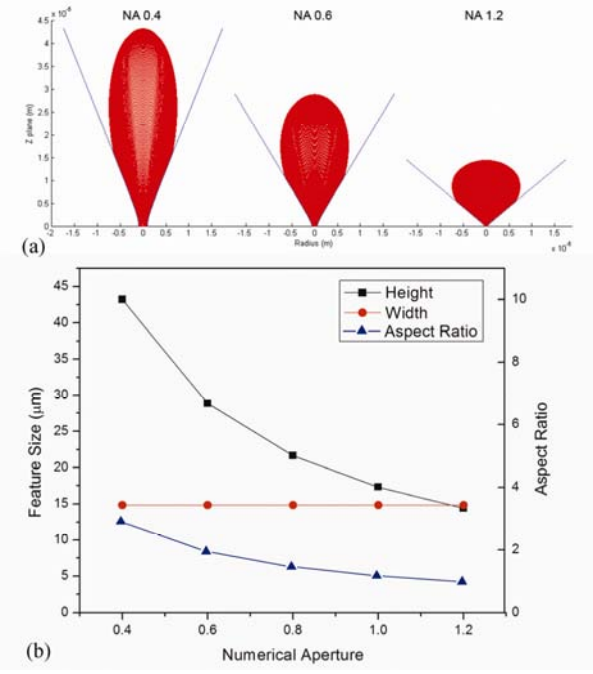

Figure 8: (a) Cross section view (b) height, width, and height/width ratio of absorption volume at different NAs (laser pulse energy of 20 μJ)

Mechanical Properties of the Welding

Fig.9 shows the reflective DIC optical image of a nanoindentation array on the cross section of a transmission welding line of two borosilicate glass plates with the processing condition of 10 μJ laser pulse energy and 0.02 mm/s laser scanning speed. The indents at 100 nm depth with a spatial resolution of 3 μm covered both unaffected and welding region. The representative curves of indents from reference region and inside the transmission welding seam were illustrated in Fig. 10. At same maximum indentation depth, the maximum load of the indent performed in the unaffected region is greater, and its residual depth is shallower. These curves imply that the mechanical properties in transmission welding region are changed from its original properties. However, in order to understand how those mechanical properties change, and how they relate to the welding strength, the spatially resolved determination and indentation fracture will be drawn into consideration.

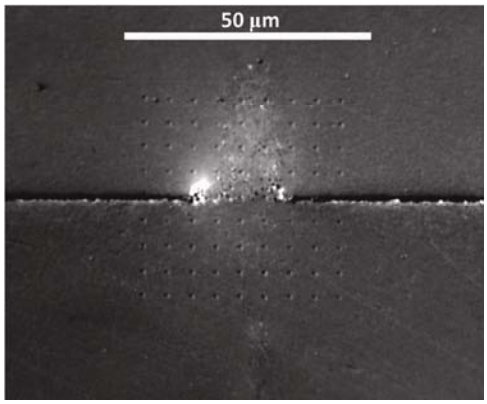

Figure 9: Reflective DIC optical image of spatially resolved nanoindentation array (100nm depth and 3 μm spacing) on the cross section (x-z plane) of a welding seam in Fig. 2.

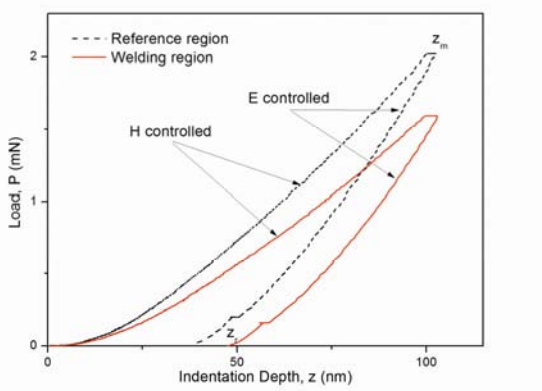

Figure 10: Representative load-displacement curves for 100 nm depth nanoindents in the welding and reference regions of borosilicate glass.

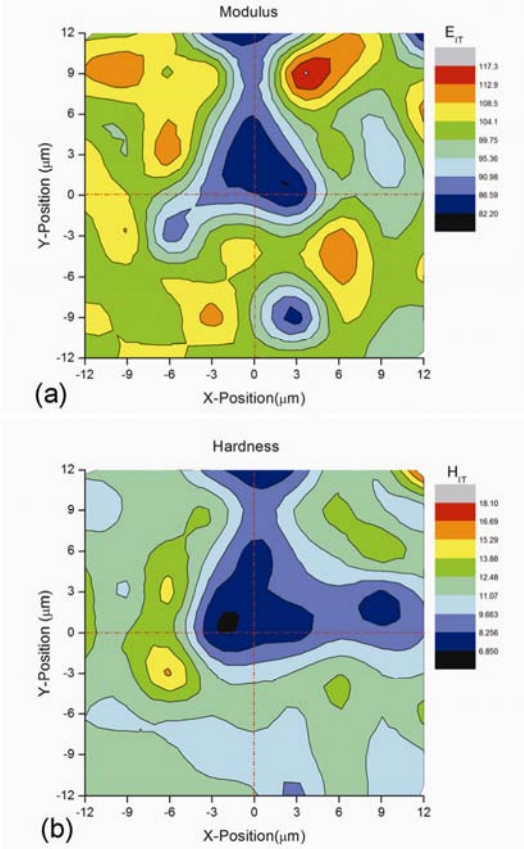

Figure 11: Spatially resolved determination of (a) Young's modulus (b) hardness contour on the cross section of welding region. The contour maps correspond to the array of 100 nm depth nanoindents with 3 μm spacing shown in Fig. 9.

Fig. 11(a) and Fig. 11(b) illustrate the contour plots of Young's modulus and hardness values corresponding to all indents in Fig. 9. The horizontal lines on the contour plots represent the welding interface while the vertical lines represent the center of welding cross section. From the contour plots, compared to their original values, the Young's modulus and hardness in the welding region are both decreased. Repeatedly heating and quenching, the material in the welding region will experience high temperature and high pressure. The presence of breaks in the linkage within a structure due to high pressure allows easier displacement of the atoms and reduces elastic modulus [21]. The hardness of glasses is determined by the strength of the bonds forming the network and by the structure of the glass [19]; therefore, due to the high pressure effect, the hardness would also be decreased as well.

Fig. 12 (a) and Fig. 12(b) show the variation of Young's modulus and hardness along the vertical line across the welding seam. The dash-dot lines on figures represent the interface of two borosilicate glass plates, and the values on right hand side of these lines represent the material properties in the top piece. The Young's modulus and hardness of affected region near the interface are as low as the welding material at interface, however, from these plots, they revealed that the affected region in the top piece is larger than the bottom piece. This could be due to the effect of the air gap at the interface. It could possibly reflect out some fraction of laser energy, and obstruct some breakdown points in the bottom piece of material. Therefore, the energy is less coupled into the bottom portion of the absorption volume, and there is less variation in mechanical properties in the bottom piece region that distance away from the interface.

Fig. 13 shows the contour of E/H ratios corresponding to the indents in Fig. 9. It is very obvious that the E/H ratios are increased in the transmission welding region. From indentation analysis, higher E/H corresponds to higher residual field intensity, implying a weaker elastic recovery and thus less pronounced radial crack extension during unloading half-cycle [20]. Therefore, the E/H ratio of material could be directly related to the fracture toughness of material. Higher E/H ratio

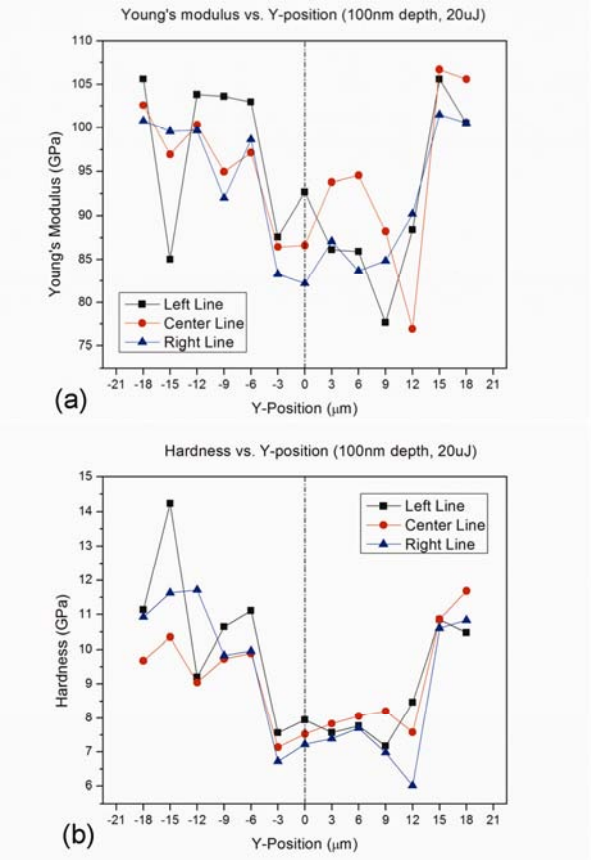

Figure 12: The variation of (a) Young's modulus (b) hardness along the vertical line across the welding seam (laser pulse energy of 20 μJ, scanning speed of 0.02 mm/s.) The dash-dot lines represent the interface of two borosilicate glass plates.

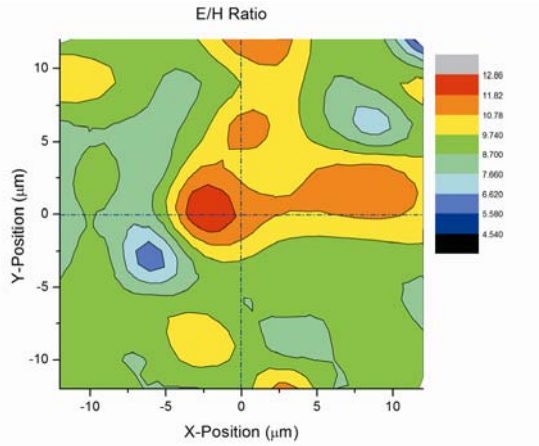

Figure 13: Spatially resolved determination of the ratio between Young's modulus and hardness (E/H) on the cross section of welding region. The contour maps correspond to the array of 100 nm depth nanoindents with 3 μm spacing shown in Fig. 9.

may lead to higher fracture toughness. To confirm the effect of increasing E/H ratio in transmission welding region, indents at greater depth were carried out to induce the radial cracks at the corners of nanoindentation imprints. Fig. 14 shows the DIC optical image of cracks induced by a bigger nanoindent. The bottom corner of nanoindentation imprint is within the welding region, and the crack at the bottom corner extended across the welding at interface of two borosilicate glass plates. Comparing the crack lengths at three corners or the nanoindentation imprints in Fig. 15, it is very obvious that the crack length in the welding region is shorter than in crack lengths in unaffected region. Using Eq. (8), due to higher E/H ratio and shorter crack length in the transmission welding region, it can be confirmed that the fracture toughness of material inside welding region is increased corresponding to the experimental results using double torsion test studied by Borrelli et al. [9]. This could be implied that the fracture strength of material in welding region is higher than the unaffected region assuming the same size of initial flaw in material.

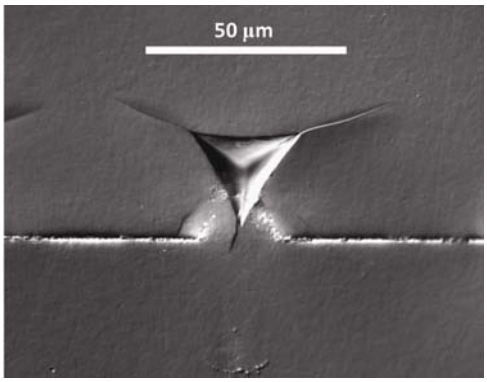

Figure 14: Reflective DIC optical microscopy of intentation fracture on cross section of a welding seam (laser pulse energy of 30 μJ, scanning speed of 0.02 mm/s, repetition rate of 1 kHz.)

Conclusion

The transmission welding on the interface of two borosilicate glass plates with standard flatness was performed by using low repetition rate femtosecond laser. The laser pulse energy that applied is high enough to cause non-linear absorption and induce breakdown in the material. The welding morphology was investigated, and it can be observed that the welding width is equivalent to the feature width of laser radiation inside single piece transparent material. Increasing laser pulse energy, the width of welding line will be larger; however, it should not be too high to induce cracks. Numerical model was explored to investigate size and shape of the absorption volume as a function of laser pulse energy and numerical aperture of an objective lens, and it could be used to predict the welding width. Spatially resolved measurements revealed the change in mechanical properties inside the welding region, and there is decrease in Young's modulus and hardness from its initial value. However, the E/H ratio is increased, and it enhances the fracture toughness of material inside welding region implying the fracture strength of the weld is higher than that of unaffected region.

References

[1] Watanabe, W., Onda, S., Tamaki, T. & Itoh, K. (2007) Joining of transparent materials by femtosecond laser pulses, Proc. of SPIE Vol. 6460, 646017-1-6.

[2] Tamaki, T., Watanabe, W., Nishii, J. & Itoh, K. (2005) Welding of transparent materials using femtosecond laser pulses, Japanese Journal of Applied Physics, 44(22), L687-L689.

[3] Watanabe, W., Onda, S., Tamaki, T., Itoh, K. & Nishii, J. (2007) Space-selective laser joining of dissimilar transparent materials using femtosecond laser pulses, Applied Physics Letters, 89, 021106-1-3.

[4] Tamaki, T., Watanabe, W. & Itoh, K. (2006) Laser micro-welding of transparent materials by a localized heat accumulation effect using a femtosecond fiber laser at 1558 nm, Optics Express, 14(22), 10468-10476.

[5] Bovatsek, J., Arai, A. & Schaffer, C.B. (2006) Three-dimensional micromachining inside transparent materials using femtosecond laser pulses: new applications, in CLEO/QELS and PhAST, California, USA, 1-2.

[6] Miyamoto, I., Horn, A. & Gottmann, J. (2007) Local melting of glass material and its application to direct fusion welding by ps-laser pulses, Journal of Laser Micro/Nanoengineering, 2(1), 7-14.

[7] Horn, A., Mingareev, I., Werth, A., Kachel, M. & Brenk, U. (2008) Investigations on ultrafast welding of glass-glass and glass-silicon, Applied Physics A, 93, 171-175.

[8] Miyamoto, I., Horn, A., Gottmann, J., Wortmann, D., Mingareev, I., Yoshino, F., Schmidt, M., Bechtold, P., Okamoto, Y., Uno, Y. & Herrmann, T. (2008) Novel fusion welding technology of glass using ultrashort pulse lasers, in Proc. 27th International Congress on Applications on Lasers & Electro-Optics, Temecula, CA, USA, 112-121.

[9] Borrelli, N., Helfinstine, J., Price, J., Schroeder, J., Streltsov, A. & Westbrook, J. (2008) Glass strengthening with an ultrafast laser, in Proc. 27th International Congress on Applications on Lasers & Electro-Optics, Temecula, CA, USA, 185-189.

[10] Bellouard, Y., Colomb, T., Depeursinge, C., Dugan, M., Said, A.A. & Bado, P. (2006) Nanoindentation and birefringence measurements on fused silica specimen exposed to low-energy femtosecond pulses, Optics Express, 14(18), 8360-8366.

[11] Kongsuwan, P., Wang, H., Vukelic, S. & Yao, Y.L. (2009) Characterization of morphology and mechanical properties of glass interior irradiated by femtosecond laser, in Proc. 28th International Congress on Applications on Lasers & Electro-Optics, Orlando, FL, USA, 1214-1223.

[12] Schaffer, C.B., Jamison, A.O. & Mazur, E. (2004) Morphology of femtosecond laser-induced structural changes in bulk transparent materials, Applied Physics Letters, 84(9), 1441-1443.

[13] Miyamoto, I., Horn, A., Gottmann, J., Wortmann, D. & Yoshino, F. (2007) Fusion welding of glass using femtosecond laser pulses with high-repetition rates, Journal of Laser Micro/Nanoengineering, 2(1), 57-63.

[14] Hallo, L., Mezel, C., Bourgeade A., Hebert, D., Gamaly, E.G. & Juodkazis, S. (2010) Laser-matter interaction in transparent materials: confined micro-explosion and jet formation, in Hall, T.J., & Gaponenko, S.V. (ed) Extreme Photonics & Applications, Springer Science, 121-146.

[15] Gamaly, E.G., Juodkazis, S., Nishimura, K., Misawa, H., Luther-Davies, B., Hallo, L., Nicolai, P. & Tikhonchuk, V.T. (2006) Laser-matter interaction in the bulk of a transparent solid: confined microexplosion and void formation, Physical Review B, 73, 214101-1-15.

[16] Kitchener, J.A. & Prosser, A.P. (1957) Direct measurement of the long-range van der waals forces, in Proceedings of the Royal Society of London, 403-409.

[17] Gere, J.M., & Timoshenko, S.P. (1990) Mechanics of Materials, PWS-Kent Pub. Co., 912pp.

[18] Zarzycki, J. (1991) Glasses and the Vitreous State, Cambridge University Press, 505pp.

[19] Varshneya, A.K. (1994) Fundamentals of Inorganic Glasses, Academic Press, 570pp.

[20] Lawn, B.R. (1993) Fracture of brittle solids, Cambridge University Press, 378pp.

[21] Shelby, J.E. (1997) Introduction to Glass Science and Technology, The Royal Society of Chemistry, 244pp.

[22] Leong, K.H. & Sanders, P.G. (2001) Welding data summary, in Ready, J.F. (ed) Handbook of Laser Material Processing, LIA, 375-379.

[23] Hallo, L., Bourgeade, A., Tikhonchuk, V.T., Mezel, C. & Breil, J. (2007) Model and numerical simulations of the propagation and absorption of a short laser pulse in a transparent dielectric material: blast-wave launch and civity formation, Physical Review B, 76, 024101-1-12.

[24] Kern, W. (1990) The evolution of silicon wafer cleaning technology, Journal of Electrochemical Society, 137(6), 1887-1892 .

[25] Zipfel, W.R., Williams, R.M. & Webb, W.W. (2003) Nonlinear magic: multiphoton microscopy in the biosciences, Nature Biotechnology, 21(11), 1369-1377.

Meet the Authors

Panjawat Kongsuwan received his M.S. from Columbia University. He is currently a doctoral student at the Manufacturing Research Laboratory at Columbia University.

Dr. Y. Lawrence Yao is currently department chair of Columbia University's Mechanical Engineering Department and director of the Manufacturing Research Laboratory. He received his Ph.D from the University of Wisconsin-Madison in 1988. He also serves on the Board of Directors of LIA.